We are IntechOpen, the world's leading publisher of Open Access books
Built by scientists, for scientists

6,900
Open access books available

186,000
International authors and editors

200M
Downloads

154
Countries delivered to

Our authors are among the

TOP 1%
most cited scientists

12.2%
Contributors from top 500 universities

CLARIVATE ANALYTICS
BOOK CITATION INDEX
INDEXED

WEB OF SCIENCE™

Selection of our books indexed in the Book Citation Index
in Web of Science™ Core Collection (BKCI)

Interested in publishing with us?
Contact book.department@intechopen.com

Numbers displayed above are based on latest data collected.
For more information visit www.intechopen.com

Nonlinear Truss-Based Finite Element Methods for Catenary-Like Structures

Jose Rodolfo Chreim and Joao Lucas Dozzi Dantas

Abstract

This chapter is devoted to an application of a finite element method formulation to forecast the static and mechanical behavior of catenary-like structures subject to general force distributions, whose development was motivated by the need of installing assemblies of containment structures, called log boom lines, upstream a hydroelectric power plant to protect its integrity from the threats that logs carried through the river pose on it. Each log boom is modeled by a tridimensional truss element and the entire lines by assemblages of trusses. While the external forces, modeled with the aid of both simulations from computational fluid dynamics and experiments from a towing tank, originate from both the river stream and the logs that accumulate through the extension of the lines, the internal forces are calculated from classic expressions of solid mechanics; hence, the numerical method imposes equilibrium between them, which ultimately defines the geometry assembly. Verification and validation were performed at both model and prototype scales, and the results corroborated the accuracy of the tool for a series of flow conditions.

Keywords: finite element method, fluid-structure interaction, containment grids, catenary-like, numerical simulation

1. Introduction

The operation of a hydroelectric power plant at the Madeira River is compromised due to the presence of many logs carried through the water stream that can damage the power plant machinery and reduce its production efficiency. To prevent such damage, nine assemblies of containment structures, called log booms (**Figures 1** and **2**), were installed near the power plant and across the river to retain and deflect these logs. Nevertheless, as the influence of logs and stream can exert large loads over the assemblies, they are under the risk of structural failure; so a numerical tool based on the finite element method (FEM) was developed to predict the distributions of loads and equilibrium configurations of the lines, therefore assisting their surveillance and maintenance. The numerical tool was part of a research and development (R&D) project developed by the Institute for Technological Research (IPT), and it can be extended to similar problems in which the structures behave likewise, as is the case of fishing nets and cleaning structures [1]. Moreover, while commercial software could be used for the same purpose, the intrinsic drawbacks of large computation time, automation, and customization
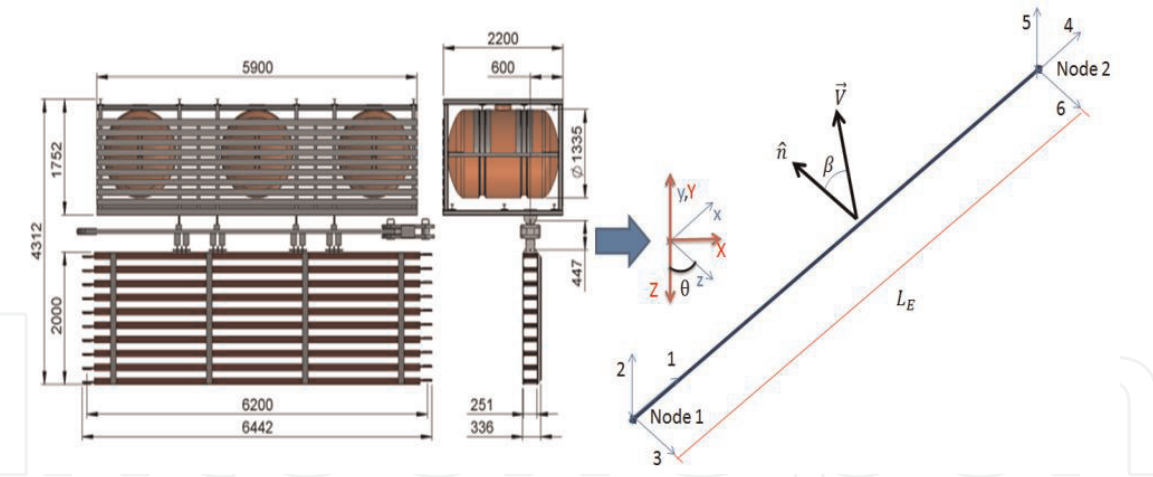
Figure 1.
Log boom unit schematics and its truss element representation with six DoF. The local reference frame is in blue, while the global in red.
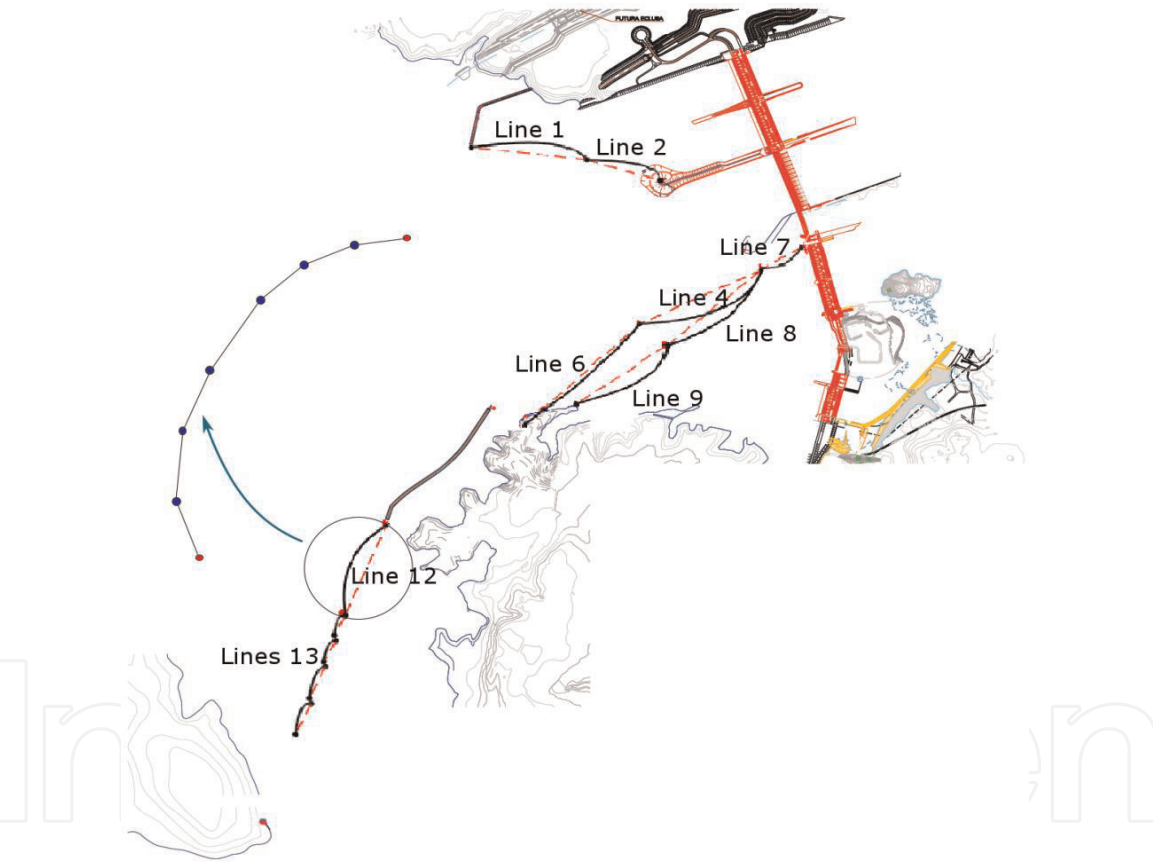

Figure 2.
Log boom lines and example of assembly of trusses used to model them.

difficulties were generally not justified by the potential increase in accuracy, as the tool would eventually be integrated in a larger numerical simulator.

2. Numerical model

The mathematical model used in the present formulation is based on the works of Felippa and Gavin [2–4], whereas the numerical implementation was developed within the Matrix Laboratory (MATLAB) environment [5]. The material deformations are assumed elastic only (i.e., no plasticity or yielding) as each log boom is

mainly composed of steel, making the unit respond linearly until approximately 80% of the yield stress [6], but the displacements are geometrically nonlinear, as the forces, the geometric stiffness, and the assembly equilibrium configuration depend on one another.

2.1 Mathematical model

Consider the three-dimensional truss element composed by six degrees of freedom (DoF) that represent all the possible translation directions its nodes have. Such element is used to model the structural behavior of each log boom (**Figure 1**).

With this numbering, the element constitutive stiffness matrix $\mathbf{K_{Ee}}$ is

$$\mathbf{K_{Ee}} = \frac{E_e A_\phi}{L_0} \begin{bmatrix} 1 & 0 & 0 & -1 & 0 & 0 \\ 0 & 0 & 0 & 0 & 0 & 0 \\ 0 & 0 & 0 & 0 & 0 & 0 \\ -1 & 0 & 0 & 1 & 0 & 0 \\ 0 & 0 & 0 & 0 & 0 & 0 \\ 0 & 0 & 0 & 0 & 0 & 0 \end{bmatrix} \tag{1}$$

while its geometric stiffness matrix $\mathbf{K_{Ge}}$ is

$$\mathbf{K_{G_e}} = \frac{T}{L_0} \begin{bmatrix} 0 & 0 & 0 & 0 & 0 & 0 \\ 0 & 1 & 0 & 0 & -1 & 0 \\ 0 & 0 & 1 & 0 & 0 & -1 \\ 0 & 0 & 0 & 0 & 0 & 0 \\ 0 & -1 & 0 & 0 & 1 & 0 \\ 0 & 0 & -1 & 0 & 0 & 1 \end{bmatrix} \tag{2}$$

These matrices represent the stiffness of the truss due to its constitutiveness (as $\mathbf{K_{Ee}}$ depends on the stiffness module E_e, on the cross-sectional area A_ϕ, and on the undeformed length L_0) and existence of external influence (counterbalanced by the tension T). Consequently, the tangential element matrix $\mathbf{K_{Te}}$, defined as the overall stiffness, is simply their sum:

$$\mathbf{K_{Te}} = \mathbf{K_{Ee}} + \mathbf{K_{Ge}} \tag{3}$$

An assembly is then modeled by the joint of $\mathbf{N}$ trusses, representing its $\mathbf{N}$ log booms, as in **Figure 2**; thus, to account for the assembly overall stiffness $\mathbf{K_T}$, each $\mathbf{K_{Te}}$ is linearly transformed from the truss local coordinate systems to the global assembly counterpart, and they are later superimposed.

Now, considering a function $\mathbf{g(u)}$ that represents the unbalance between internal and external forces ($\mathbf{F}$ and $\mathbf{R}$, respectively), for a given geometric configuration $\mathbf{u}$, there is a relation between $\mathbf{g(u)}$ and $\mathbf{K_T}$:

$$g(u) \equiv R - F = K_T \Delta u \tag{4}$$

The equilibrium configuration $\mathbf{u}^*$ is achieved when $\mathbf{g(u)}=\mathbf{0}$, and in order to find it, $\mathbf{g(u}^*)$ can be expanded into a Taylor series about an arbitrary initial configuration $\mathbf{u^j}$:

$$g(u^*) = g(u^j) + \frac{dg(u)}{du}\bigg|_{u = u^j}(u^* - u^j) + \frac{1}{2}\frac{d^2\,g(u)}{du^2}\bigg|_{u = u^j}(u^* - u^j)^2 + O(u^3) = 0$$

$$(5)$$

Truncating Eq. (5) to the first order, $\mathbf{u}^*$ can be approximated by the unbalance and its first derivative:

$$u^* \approx u^j - \left(\frac{d\,g(u)}{du}\bigg|_{u = u^j}\right)^{-1}g(u^j)$$

$$(6)$$

which, however, is a linear approximation of this nonlinear formulation. Given such nonlinearity, the problem must be solved numerically, and all the equations presented insofar are part of an iterative scheme, in which $\mathbf{j}$ ($\mathbf{j=0, 1, ...}$) is the $\mathbf{j^{th}}$ iteration. Therefore, numerically speaking, successive expansions must be taken about the consecutive values of $\mathbf{u}$ until a satisfactory equilibrium $\mathbf{u^{*\,Num}}$ is achieved within a specified tolerance. So, from Eq. (6), at each iteration an improved equilibrium configuration $\mathbf{u^{j+1}}$ is obtained. Also, rearranging Eq. (4) in terms of the same improved equilibrium configuration, one obtains:

$$u^{j+1} = u^j - \left[K_T^j\right]^{-1}(R^j - F^j)$$

$$(7)$$

As expected, by similarity, $\mathbf{K_T^j = \frac{d\,g(u)}{du}\big|_{u=u^j}}$, i.e., the tangential matrix is a function of $\mathbf{u^j}$. So, the numerical method consists of starting from an initial geometry, calculating the external and internal forces, calculating the assembly tangential matrix, and updating the geometric configuration. This process is repeated until the internal and external forces are sufficiently close.

2.2 Force calculations

The loads acting on the assembly originate from the hydrodynamic interaction and from the log accumulation and must be counterbalanced by the internal forces, which are a function of the mechanical properties of the material. Although the formulation is tridimensional, for the purposes by which the model was made, it is sufficient to obtain the equilibrium configuration on the XZ plane. Hence, the calculations presented next will only be on this plane.

2.2.1 External loads

To estimate the external forces, a database was created with the aid of computational fluid dynamics (CFD) (**Figure 3**). The software Siemens Star-CCM+, version 12.02.011, was used for these numerical simulations: both water and air were admitted incompressible, and the flow field was modeled using the unsteady Reynolds-averaged Navier-Stokes equations implicitly (at the first iterations, the movements were frozen to ensure fluid stabilization and then gradually released, still seeking stabilization); the interaction between the fluids was represented by the volume of fluid Eulerian multiphase model, and the multiphase conditions were defined by the flat wave model with a numerical damping, added in the momentum equation on the vertical direction, on both the inlet and outlet boundary conditions to minimize the effects of reflection and ensure better convergence; finally, the k-ω SST model was adopted.
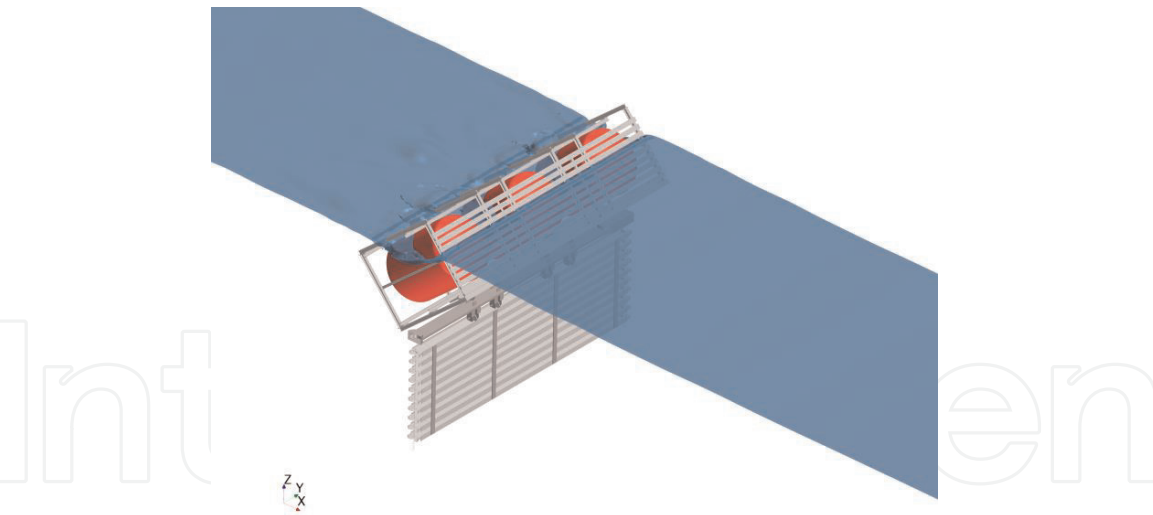
Figure 3.
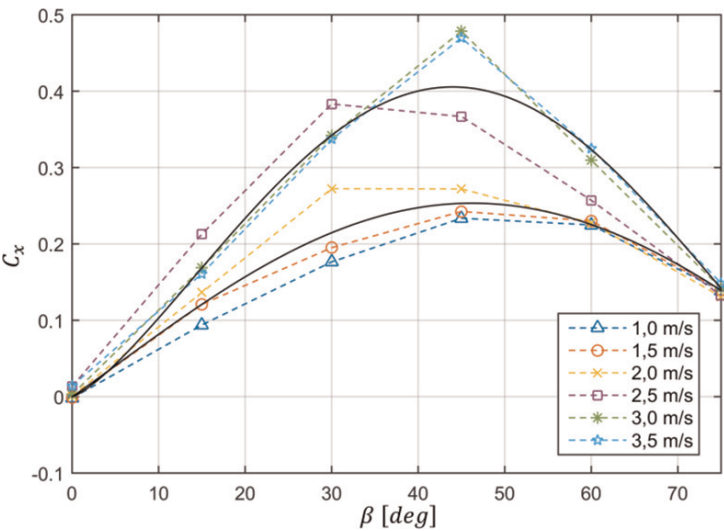*CFD domain used to obtain the external force database.*

Figure 4.
Example of C_x and C_z coefficients as functions of the velocity magnitude and incidence angle.

A series of velocity magnitudes **V** and incidence angles **β** were simulated such that normal and tangential coefficients (C_z and C_x, respectively) were calculated [7–9]. From them, fitting curves in the form of Eq. (8) were adjusted, whose values of **K** depend on **V** (**Figure 4**):

$$C_x = K_{1x} \cos (K_{2x}\beta)^{K_{3x}}$$

$$C_z = K_{1z} \text{sen}(K_{2z}\beta)^{K_{3z}} \tag{8}$$

Each part of the log boom that is free to rotate was assigned with a pair of coefficients (i.e., the grids and the chassis) such that the total hydrodynamic force acting on the trusses is retrieved based on them. So, for the **i**[th] log boom ($i = 1, ..., N$),

$$R_{xi}(V_i, \beta_i) = \frac{1}{2}\rho V_i^2 (C_{cxi}A_{CN} + C_{Gxi}A_{GN})$$

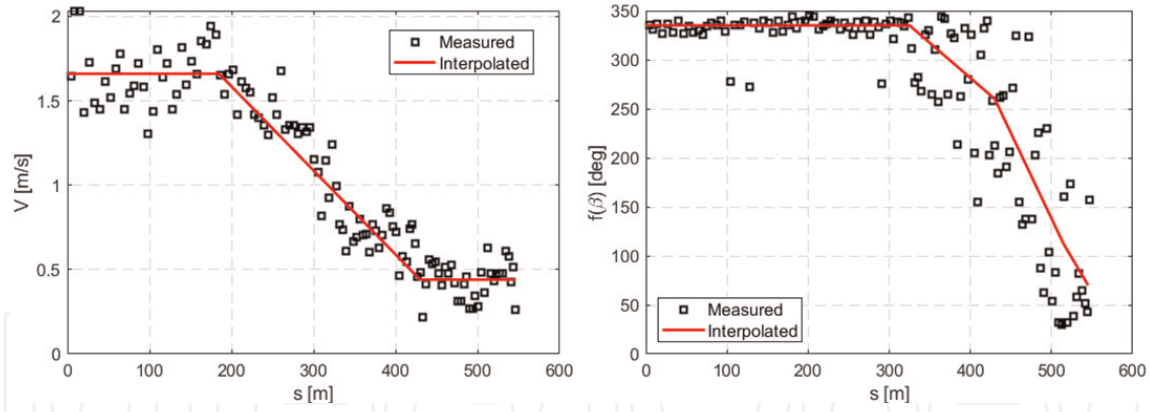$$R_{zi}(V_i, \beta_i) = \frac{1}{2}\rho V_i^2 (C_{czi}A_{CN} + C_{Gzi}A_{GN}) \tag{9}$$

Figure 5.
Example of the variation of the velocity magnitude and incidence angle along a projected line that connects the mooring points. The angles are measured taking the north coordinate of reference; thus, it is not β itself, but a function of it.

A_{CN} and A_{GN} are the chassis and grid front areas, and ρ is the water density. The **V** and **β** combinations used in the simulations were arithmetically averaged from velocimetry data measured in situ along a line **s** that connects the assemblies' mooring points (**Figure 5**).

Once the hydrodynamic coefficients were obtained, the contribution from the logs that accumulate along the lines was assumed to be increments on the normal coefficients [10] and estimated with the aid of data from experiments at the towing tank of the IPT (**Figure 6**). Thus, considering already such increments, Eq. (9) accounts for the total external forces acting on the center of the element, which are equally distributed to its nodes and further transformed from local to global coordinates as well, according to the angle θ_i between the two reference frames:

$$R_{Xi} = -R_{zi}\ \sin(\theta_i) + R_{xi}\ \cos(\theta_i)$$
$$R_{Zi} = R_{zi}\ \cos(\theta_i) + R_{xi}\ \sin(\theta_i)$$

(10)

So, $R_{Xi}/2$ and $R_{Zi}/2$ act on the **X** and **Z** directions of each node element.

2.2.2 Internal loads

The tension distribution throughout the trusses is calculated based on classic linear relations of solid mechanics, and it acts on the axial direction of the element.
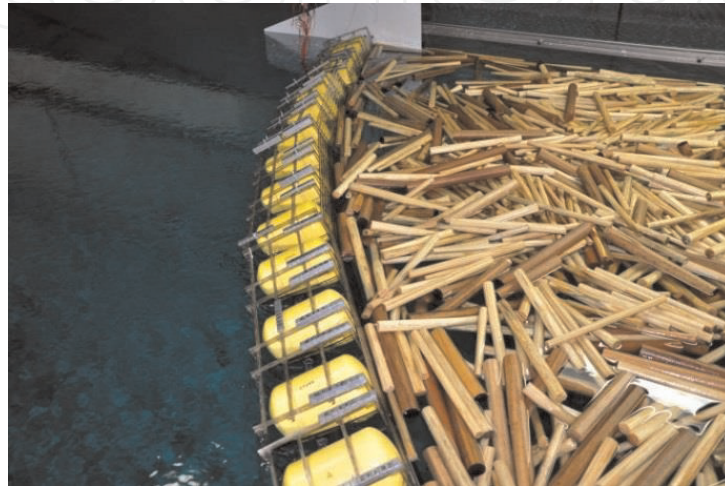

Figure 6.
Example of experiment to measure the influence of the logs on the assembly.

Therefore, for the same $\mathbf{i^{th}}$ log boom, stretched to a new length $\mathbf{L_i}$ (thus having new coordinates $\mathbf{u_i}$), the internal tension acting upon it is calculated as in Eq. (11):

$$T_i = EA_\phi \left(\frac{L_i - L_0}{L_0} \right) \tag{11}$$

This tension must be transformed to internal forces $\mathbf{F_i}$ that act on the nodes and are represented on the global coordinate system. Considering the same angle $\mathbf{\theta_i}$, the internal forces are obtained through a similar transformation:

$$\begin{aligned} F_{Xi} &= T_i \cos (\theta_i) \\ F_{Zi} &= T_i \ \sin (\theta_i) \end{aligned} \tag{12}$$

2.3 Initial condition

Originally, the solution strategy was to adopt the line completely stretched along the $\mathbf{X}$ direction and then gradually move the leftmost mooring point by small increments $\vec{\mathbf{\Delta^j}}$ toward its final location, while the rightmost mooring point would start at its correct location. Then, at each $\vec{\mathbf{\Delta^j}}$ the iterative scheme was run until convergence (**Figure 7**).

However, such quasi-static approach is computationally expensive because of the repetitiveness of the iterative procedure. Additionally, $\vec{\mathbf{\Delta^j}}$ has to be carefully chosen to avoid numerical divergence. Thus, an improved initial condition was proposed in which the assembly was initially approximated by a catenary whose "weight vector" was obtained from the average of the hydrodynamic forces along $\mathbf{s}$ (**Figure 8**). Then, with the initial geometry determined, the external and internal forces could be calculated based on node equilibrium (**Figure 9**), as in Eq. (13):

$$\vec{T}_{i-1} + \vec{T}_i + \frac{\vec{R}_{i-1} + \vec{R}_i}{2} = \vec{0} \tag{13}$$

in which $\vec{R}_i = R_{iX}\hat{X} + R_{iZ}\hat{Z}$ and $\vec{T}_{i-1}$ and $\vec{T}_i$ are not known a priori (note that there is no "element 0," but $\vec{T}_0 = \vec{T}_1$); thus, a recursive scheme starting from one of
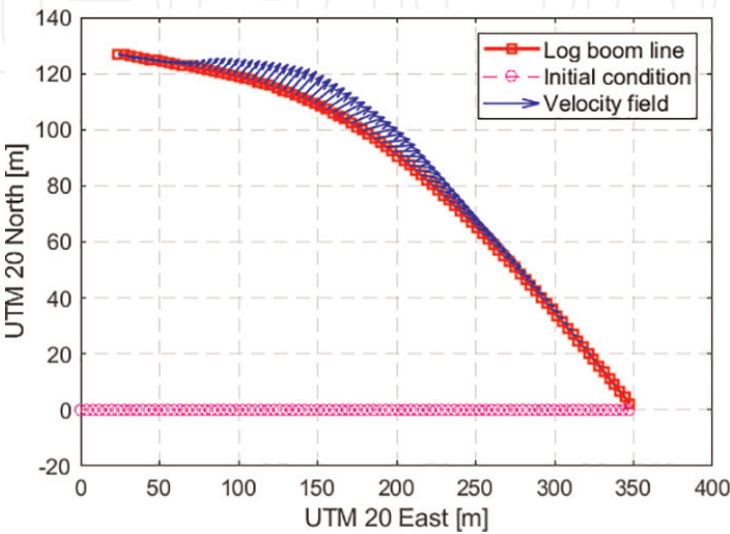

Figure 7.
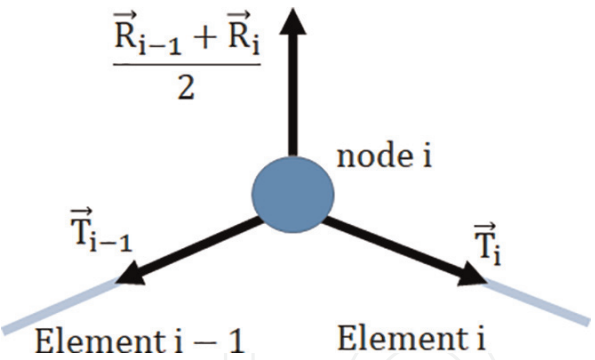*Example of initial condition and its evolution until final convergence.*

Figure 8.
Schematics of the new initial condition to obtain the tension distribution throughout the elements.
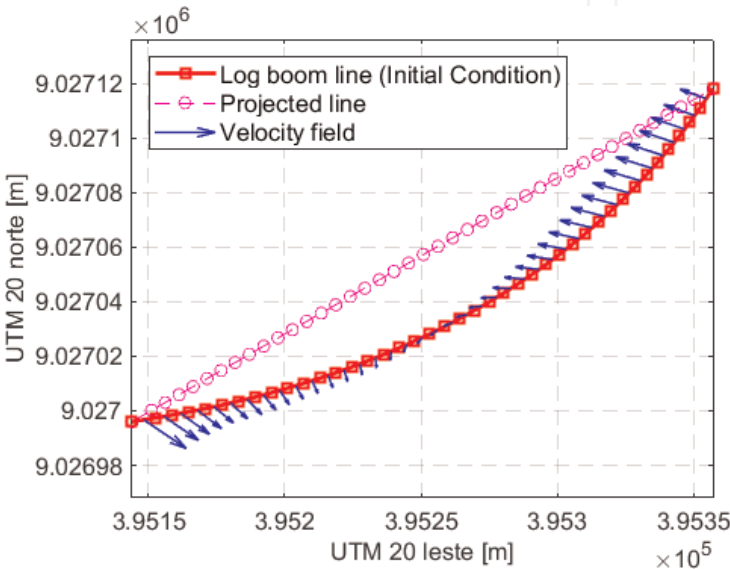

Figure 9.
Example of improved initial condition (catenary shape).

the mooring points is performed, as (13) has only one unknown at any of these locations. The internal forces are then calculated using Eq. (12), and the iterative scheme starts by either stretching the geometry by a small amount $\vec{\delta}$ from the catenary geometry or, equivalently, by creating a small unbalance **g**.

2.4 Static condensation

An intrinsic characteristic of structural problems is the presence of fixed degrees of freedom (F) in addition to the free ones (L). Thus, a common practice in FEM, known as static condensation, is to renumber the DoF seeking to reorder and split the linear system into two sub-systems. So, the displacement array can be written as:

$$\Delta u = \left\{ \begin{array}{c} \Delta u_L \\ \Delta u_F \end{array} \right\} \tag{14}$$

and the unbalance array can be similarly split:

$$g(u) = \left\{ \begin{array}{c} g(u_L) \\ g(u_F) \end{array} \right\} \tag{15}$$

For the log boom assembly, the fixed DoF are related to the mooring points, so $\Delta\mathbf{u_F}$ are their known displacements, and $\mathbf{g(u_F)}$ are the unknown reaction forces, whereas the free DoF are related to the unknown displacement of the rest of the line; $\Delta\mathbf{u_L}$ and $\mathbf{g(u_L)}$ are the known difference between the external hydrodynamic and internal loads. Thus, the linear system (Eq. (4)) can be rewritten as:

$$\left\{ \begin{matrix} \Delta u_L \\ \Delta u_F \end{matrix} \right\}^j = -\left[K_T^j \right]^{-1} \left\{ \begin{matrix} g(u_L) \\ g(u_F) \end{matrix} \right\}^j \tag{16}$$

Additionally, the matrix $\mathbf{K_T}$ can be interpreted as follows:

$$K_T = \begin{bmatrix} K_{LL} & K_{LF} \\ K_{FL} & K_{FF} \end{bmatrix} \tag{17}$$

Thus, from Eq. (4),

$$\begin{cases} K_{LL}^j \Delta u_L^j + K_{LF} \Delta u_F^j = g(u^j)_L \\ K_{FL}^j \Delta u_L^j + K_{FF}^j \Delta u_F^j = g(u^j)_F \end{cases} \tag{18}$$

These sub-systems are solved recursively: the first of Eq. (18) is solved for $\Delta\mathbf{u_L^j}$ and, sequentially, the reaction forces as calculated from the second one. Moreover, static condensation is needed regardless of the initial condition used.

2.5 Sub-relaxation

Several times, the initial condition itself is not sufficient to ensure convergence because the average velocity used to calculate the catenary "weight" might not create a representative starting geometry. So, whenever the direct method fails, a sub-relaxation parameter is applied to the force unbalance as a way to prevent large deflections through the line, which is especially interesting during the first iterations; the restrained deflections are generally sufficient to adequately converge the simulation. The sub-relaxation Ω, $0 < \Omega \leq 1$ is applied in the updating process of $\mathbf{g(u)}$ such that

$$g(u^j) = g(u^{j-1}) + \Omega^j \left(R^j - F^j \right) \tag{19}$$

Ω is usually a function of the iteration, but it must necessarily achieve unity prior to final convergence. An example of how this parameter varies with the iteration is shown in **Figure 10**.

2.6 Post-processing

After numerical convergence, a series of variables can be outputted, such as the final geometry, the velocity magnitude and incidence angle acting over each log boom, the reaction forces, and the tension distribution along the length of the line $\mathbf{L_A}$. These variables, especially the last one, are of great importance, once they help predict whether or not the simulated condition threatens the integrity of the line. Examples of converged line and tension distribution are presented on **Figures 11** and **12**.
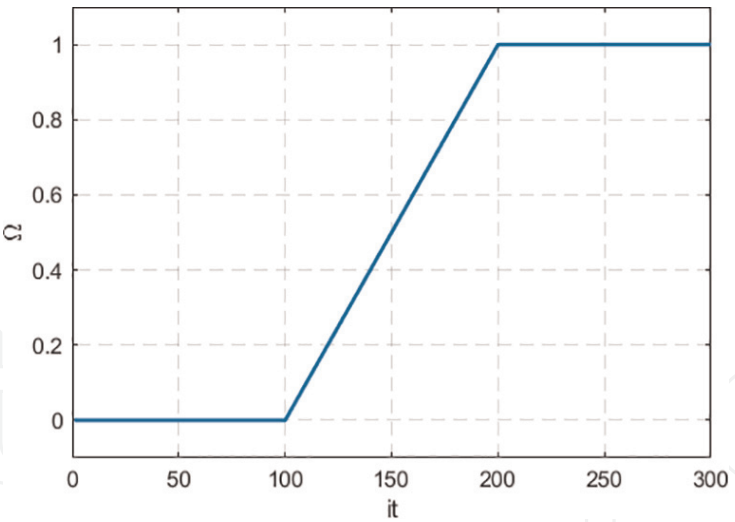
Figure 10.
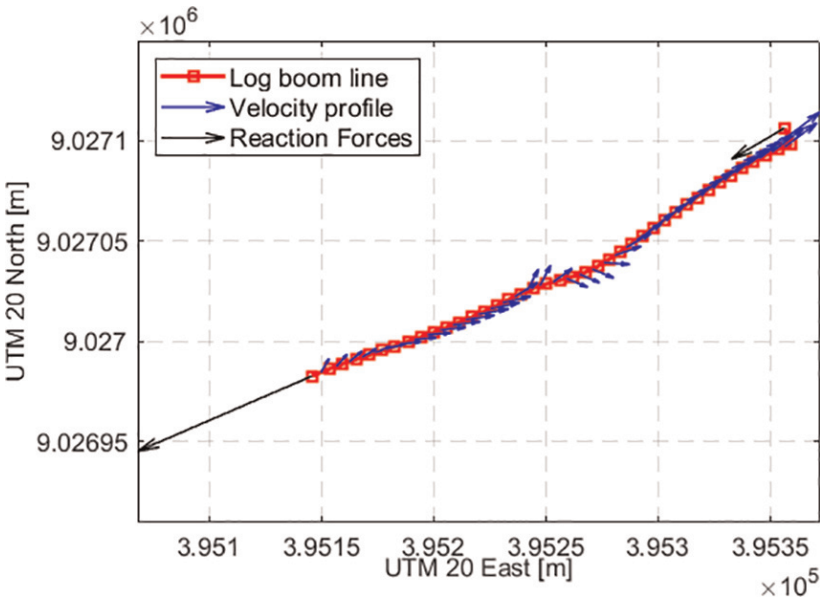*Example of Ω behavior as a function of the iteration.*

Figure 11.
Example of configuration after convergence, evidencing the final geometry, the velocity profile, and the reaction forces.
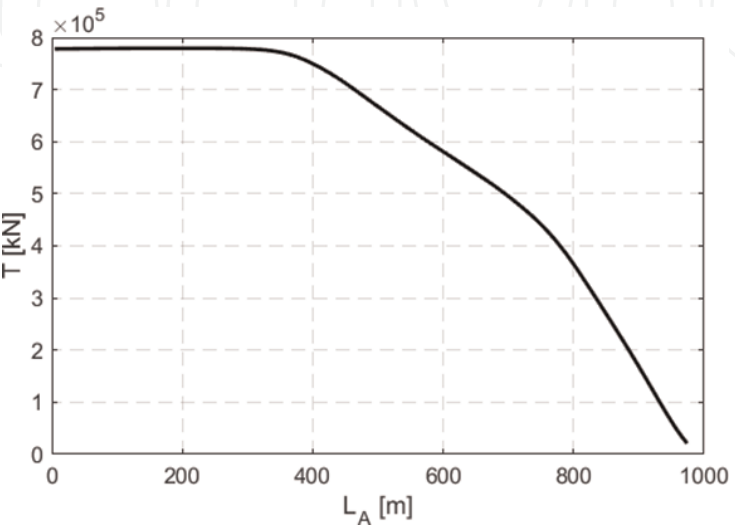

Figure 12.
Example of tension distribution along the assembly length L_A.

3. Results

In order to verify and validate the tool, thus assessing the numerical method developed, many simulations were compared to theoretical, experimental, and numerical data. As the ASME Verification & Validation Committee defines [11], validation determines the degree of accuracy that a numerical model has in representing the real world from its perspective, whereas verification evaluates its intrinsic errors and uncertainties. So, the committee states that verification precedes validation, as they must be performed to ensure the numerical reliability of the solution. In this work code and solution verifications were done by systematically refining the discretization and comparing the outputs with theoretical data from the problem of a catenary [12]. Following, the validation was done for two major cases: by comparing the solution with experimental results from a 1:10 scale model tested in the towing tank at the Naval and Ocean Engineering Laboratory of the IPT [13] and by comparing the solution with numerical simulations from SIMPACK® Multi-Body Simulation software in prototype scale [12, 14]; the later comparison had to be done against numerical data because it was unfeasible to instrument the in situ assemblies. Additionally, only hydrodynamic cases (i.e., without logs) were compared.

3.1 Verification from a theoretical catenary model

While evaluation of the error was performed through comparison with the catenary model, estimation of the error was done through classical Richardson extrapolation [12]. Code and solution verifications were performed by systematic grid refinement, with the coarsest mesh having 100 elements, the finest 800, and in between these two, successive meshes were created such that the number of trusses was consecutively increased by a value of approximately $\sqrt{2}$, as recommended by the committee [11]. For the analysis, a refinement ratio $\mathbf{r}$ that is a dimensionless form of representing the number of elements was defined:

$$r = \frac{h_N}{h_{N_{Max}}} \tag{20}$$

$\mathbf{h_N}$ is a representative grid size that, for the present formulation, assumes the form of Eq. (21):

$$h_N = \frac{\sum_{i=1}^{N} L_0}{N} = L_0 \tag{21}$$

Thus, according to Eq. (20), $\mathbf{r=1}$ represents the finest grid and $\mathbf{r=0}$ an extrapolation in which the number of elements would hypothetically tend to infinity, as their length would decrease accordingly. In the convergence region, the behavior of the solution takes the form of Eq. (23), in which $\mathbf{f_{ext}}$ is the extrapolated value, $\mathbf{p}$ the order of convergence, and $\mathbf{C}$ a constant to be determined. From this expression, a fitting curve is plotted against $\mathbf{r}$ for the assessment of the convergence behavior:

$$f(h_N) = f_{ext} + Ch_N^p \tag{22}$$

The relative error is simply evaluated by calculating the difference between the theoretical and numerical values:

$$E_r = \frac{|f_{ext} - f(h_N)|}{|f_{ext}|} \tag{23}$$

and the uncertainty σ estimated through a grid convergence index (GCI):

$$GCI = \frac{F_S|f(h_{N_{Max}}) - f(h_{(N_{Max}-1)}|}{\left[\frac{h_{N_{Max}}}{h_{(N_{Max}-1)}}\right]^P - 1} \tag{24}$$

$$\sigma = \frac{GCI}{\psi \times f_{ext}} \tag{25}$$

F_S and ψ are assigned, 1.25 and 1.1, respectively, so a safe value for σ is estimated. The catenary used for verification has a total length of $L_C = 200$ m, and the mooring points are at $(0, 200)$ and $(10, 20)$. A vertical force per unit length $F' = 617.32$ N/m acts throughout, and the minimum and maximum forces over the catenary are used as variables of verification, $f(h_N)$; they are both functions of the curve parameter a, which in turn is obtained by solving a transcendental equation that depends on the geometric parameters and on the force distribution:

$$F_{min} = a \times F' \tag{26}$$

$$F_{max} = \max\left\{\frac{l \times F'}{\sin\left[\tan^{-1}\left(\frac{l}{a}\right)\right]}\right\} \tag{27}$$

l is the length of a segment measured from one of the catenary vertices. **Figure 13** shows the trends of the numerical forces as a function of the refinement ratio along with the theoretical values, which are $F_{min} \approx 110.793$ kN and $F_{min} \approx 133.492$ kN. On both cases p is close to 1, i.e., a convergence accuracy of first order. Furthermore, the extrapolated values differ from the theoretical ones by no more than **0.2%**, and for the finest grid, the error is within the numerical uncertainty. Finally, all the values are close to the fitting curve, indicating that even for the poorest grids they seem to be within the convergence region: in fact, if the uncertainties remain of the same order regardless of the level of discretization, the disparity between the poorest grid and theoretical value is acceptable [12].

Finally, **Figure 14** shows a comparison between numerical and theoretical geometries; as they practically overlap, the verification corroborates the precision of the proposed model. As a note, in order not to be much close to the correct
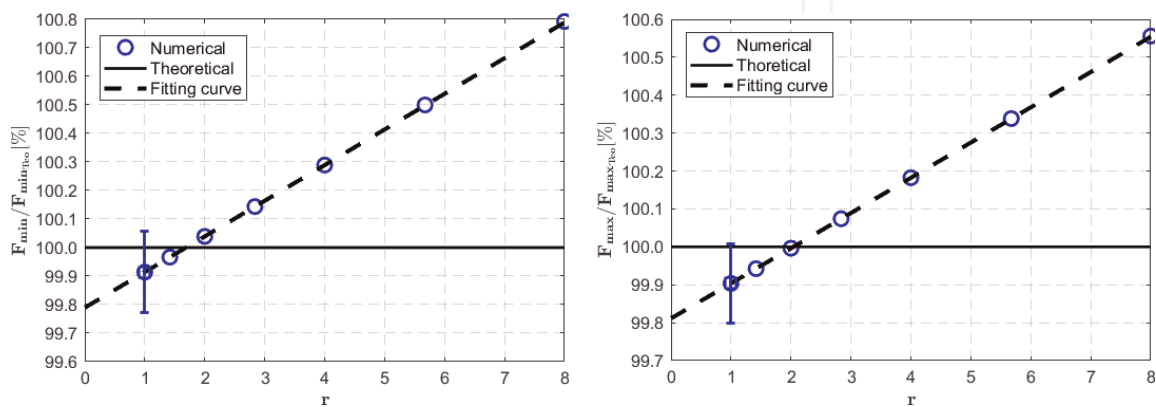
Figure 13.
Convergence of the numerical catenary maximum and minimum forces versus refinement ratio. Values are normalized by the theoretical ones.
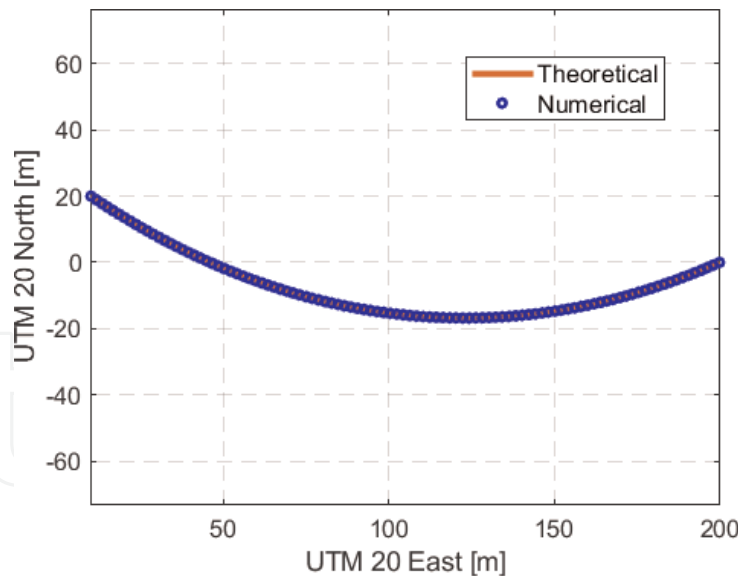
Figure 14.
Geometry comparison for the theoretical formulation and numerical method.

catenary geometry, the verification was conducted with the line completely stretched along the **X** direction.

3.2 Model scale validation

Reduced model experiments were conducted at the facilities of the IPT in a 1:10 scale with the purpose of studying the hydrodynamic behavior of such structures [13]. To do so, the model, developed mainly in polycarbonate and polymer, was constructed with the aid of a laser cutting machine and a 3D printer; the assembly was ballasted by adding lead stripes along the structure but without changing its front area as to minimize drag interference; to test both symmetric and asymmetric setups, log booms were added from a five-unit symmetric configuration, while the left mooring point was offset by distances **ΔZ** along the flow direction, since the model width was limited by the basin; flat plates were attached on both extremities to reduce the interference of the structures and to better control the flow incidence.

Four S-Type S9M uniaxial load cells, produced by HBM, were used at each extremity, each of which with a nominal measure limit of 500 N, so the tensile forces acting on the leftmost and rightmost log booms could be acquired. Additionally, to understand how the stain behaves on each log boom and also how it is transferred throughout the structure, water strain gages, manufactured by Kyowa Electronic Instruments, were placed on one of the modules, as shown schematically in **Figure 15**. These locations were appropriately chosen with the aid of numerical simulations from finite element method: the criterion was to locate the stress concentration area that increased the measurement sensitivity while avoided the high strain gradients, since the latter can contribute to unreliable measurements.

Figures 16–18 compare experimental and numerical results for three different configurations as the function of the velocity. "LE" indicates "left extremity" and "RE" "right extremity," while "Exp" and "Num" refer to experimental and numerical values. No numerical uncertainty was provided since the number of trusses was maintained equal the number of log booms.

The results agree satisfactorily: the differences are more evident as the free stream velocity increases; the numerical method reproduces the experimental observation that the tensile force is larger at the leftmost log boom, an expected trend since tensile loads are higher for elements that are parallel to the stream; the
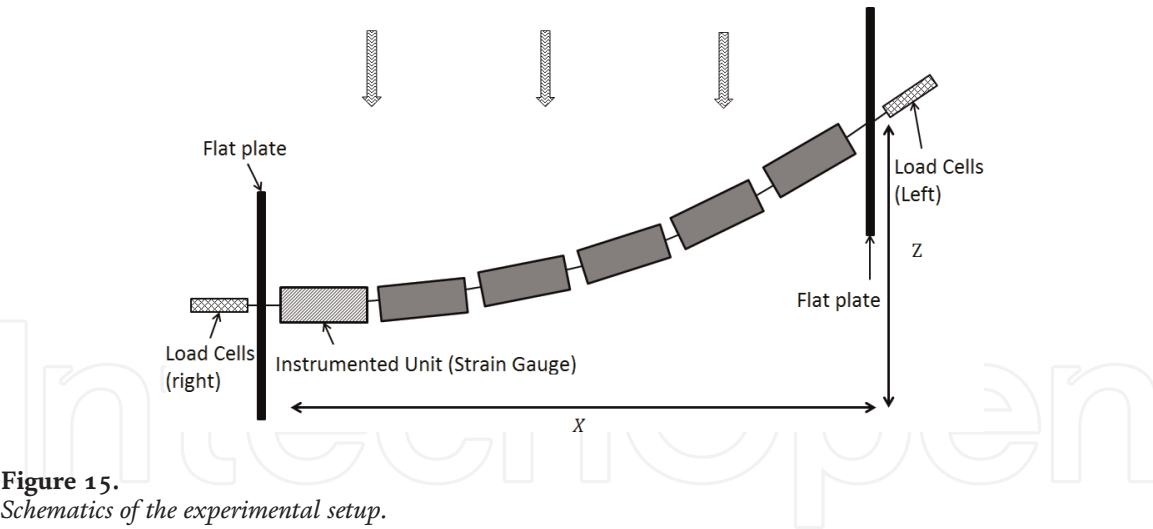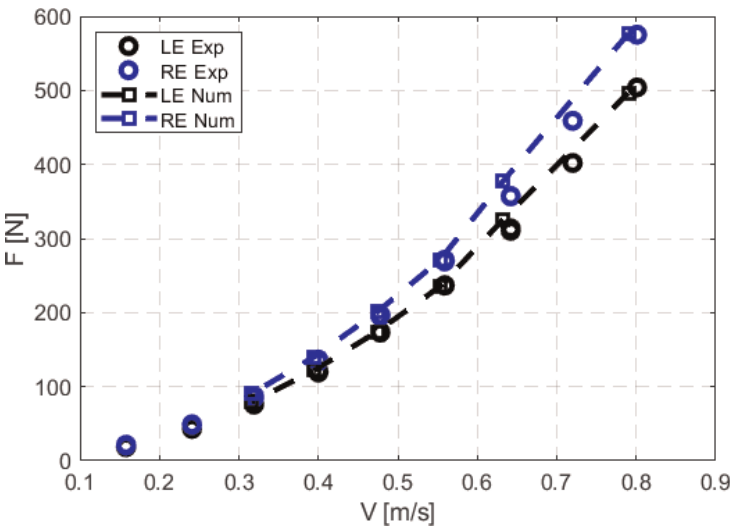
Figure 15.
Schematics of the experimental setup.

Figure 16.
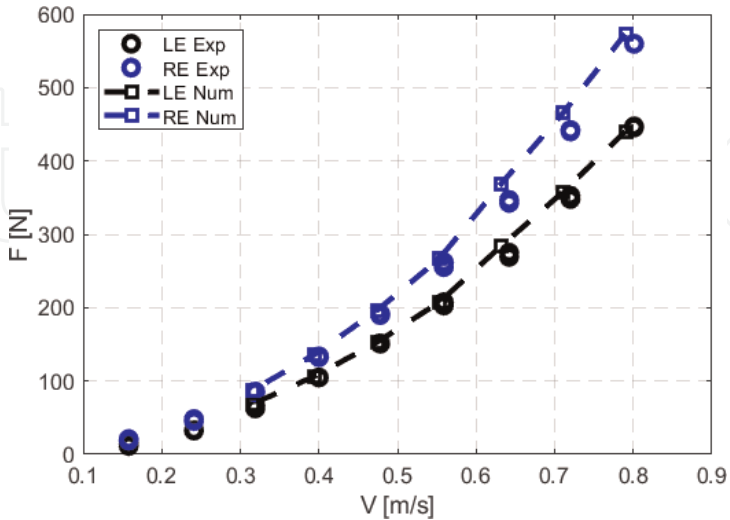*Force comparison as a function of free stream velocity. Six log boom lines.*

Figure 17.
Force comparison as a function of free stream velocity. Seven log boom lines.

number of log booms seems not to affect the accuracy of the results, as the error remains practically the same regardless of the configuration; the larger differences are within **6.0**% and are possibly due to reasons such as the model material properties, the modeling of the external forces, and the few number of elements. For the
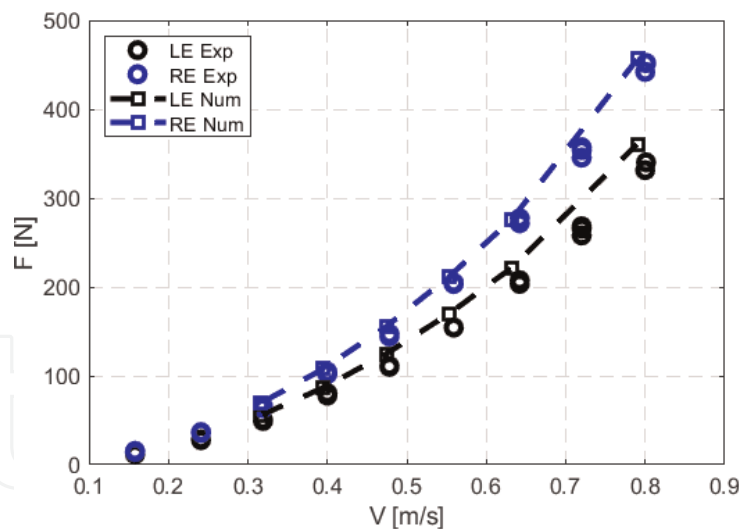
Figure 18.
Force comparison as a function of free stream velocity. Eight log boom lines.

later reason, better agreement could result from finer grids, although the one-to-one representation would be lost.

3.3 Prototype-scale validation

A prototype-scale validation is presented, and the results were compared to simulations from SIMPACK® Multi-Body Simulation software. The variables of comparison are again the reaction forces at the leftmost and rightmost anchor points, and the relative differences $\mathbf{u}_{LE}$ and $\mathbf{u}_{RE}$ use the values of SIMPACK® for normalization. In the following tables, SP refers to the results from SIMPACK®, while FEM to the results from the current method. Three validation cases were performed: line 02, line 12, and the set of line 13.

3.3.1 Line 02

The first prototype validation was performed for line 02 with a variable velocity profile, similar to the one presented in **Figure 5**. An example of converged solution for line 02 is presented in **Figure 19**, in which the equilibrium configuration, projected line, and velocity distribution are depicted.

The results from SIMPACK® and the current method are presented in [14]: the first simulation considers a 20% increase in the normal external force (C_z), while the second a 50% increase.

Table 1 shows that the maximum relative difference for the simulations that happen at the **RE** (approximately 7.6%), while for the **LE** the maximum difference is about 5.3%. Such values are satisfactory given the simplicity of the tool, in comparison to SIMPACK®.

SP (kN)		FEM (kN)		u (%)	
LE	**RE**	**LE**	**RE**	**LE**	**RE**
1025	814	1076	876	5.0	7.6
1239	1029	1305	1104	5.3	7.3

Table 1.
Comparison of results between SIMPACK® and the current method—Line 02.

3.3.2 Line 12

The second validation was performed for line 12 with several velocity profiles, also similar to the one presented in **Figure 5**. Analogously, **Figures 19** and **20** depict an example of a converged solution.

Table 2 presents the comparison between SIMPACK® and the developed formulation. For this set of simulations, the maximum percentage difference happens at the **LE**, and its value is approximately 6.6%, while at the **RE** this difference is about 5.2%; the values are comparable to those for line 02, except that the extremities at which the maximum occurs are swapped.

3.3.3 Lines 13

The last validation was conducted for the group of lines 13, i.e., for lines 13A, 13B, 13C, and 13D. **Figure 21** is an example of a converged simulation for line 13C/13D.
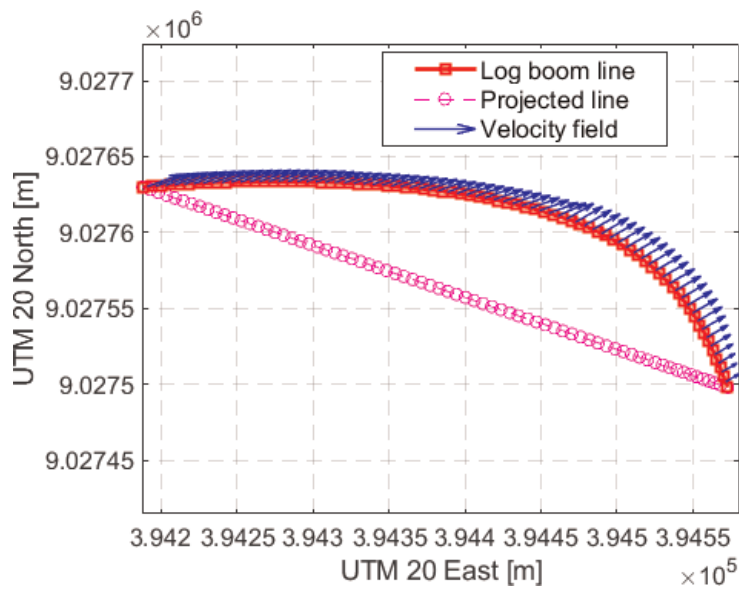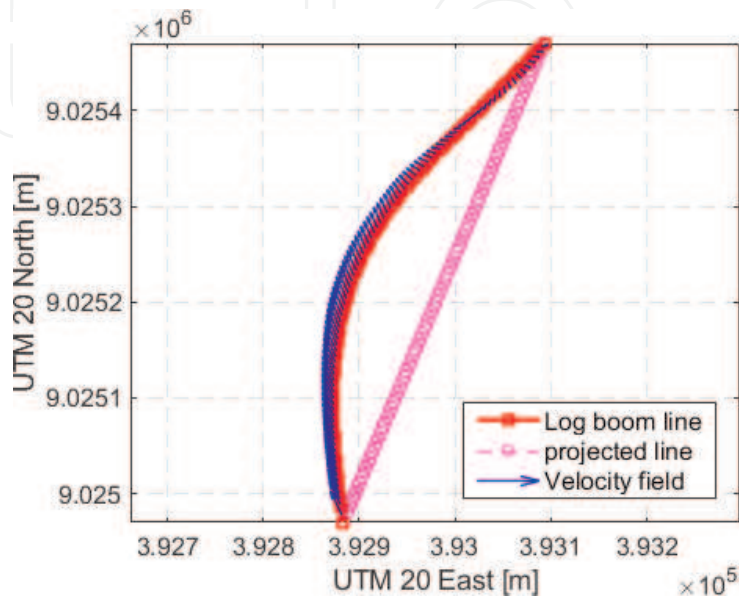

Figure 19.
Example of converged simulation for line 02.

Figure 20.
Example of converged solution for line 12.

SP (kN)		FEM (kN)		u (%)	
LE	RE	LE	RE	LE	RE
1566	1234	1666	1295	6.4	4.9
1540	1204	1641	1267	6.6	5.2
1866	1479	1983	1543	6.3	4.3
2028	1578	2158	1659	6.4	5.2
1463	1124	1559	1181	6.6	5.1
1793	1387	1910	1459	6.5	5.2
1946	1487	2071	1564	6.4	5.2
1789	1382	1905	1454	6.5	5.2
1767	1359	1877	1424	6.2	4.8
1710	1306	1821	1374	6.5	5.2
2255	1748	2405	1840	6.6	5.3
1701	1314	1811	1381	6.4	5.1
1820	1414	1888	1425	3.7	0.8

Table 2.
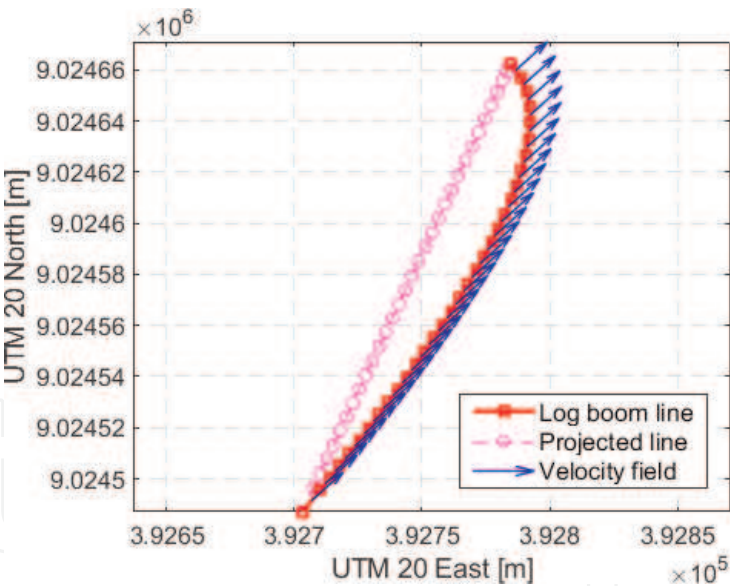*Comparison of results between SIMPACK® and the current method—Line 12.*

Figure 21.
Example of converged solution for line 13C/13D.

Particularly for line 13, the magnitude and incidence angle remained constant throughout them, varying from simulation to simulation. In **Table 3** these parameters are summarized: the first columns indicate the velocity range (VR) used in each simulation for the choice of the coefficients of Eq. (8), even though the actual velocity magnitude was sometimes not within that range.

Table 4 presents the comparison between SIMPACK® and the developed formulation.

The maximum percentage difference of the simulations happens again at the **LE** and is approximately 7.0% for line 13A/13B and 7.1% for line 13C/13D. At the **RE**, the difference is about 5.5% for line 13A/13B and 6.3% for line 13C/13D.

	Line 13A/13B		Line 13C/13D	
VR (m/s)	**V (m/s)**	**Angle (°)**	**V (m/s)**	**Angle (°)**
2.5 < V < 3.5	3.18	54.44	2.11	59.60
2.5 < V < 3.5	2.49	54.81	2.04	42.00
1.0 < V < 3.5	2.14	52.11	1.60	56.26
1.0 < V < 3.5	1.80	49.56	1.33	42.48
1.0 < V < 2.0	1.69	53.06	1.13	61.03
1.0 < V < 2.0	1.36	52.80	1.05	43.53

Table 3.
Parameters for simulations of lines 13.

Line 13A/13B						Line 13C/13D					
SP (kN)		**FEM (kN)**		**u (%)**		**SP (kN)**		**FEM (kN)**		**u (%)**	
LE	**RE**	**LE**	**RE**	u_{LE}	u_{RE}	**LE**	**RE**	**LE**	**RE**	u_{LE}	u_{RE}
1550	1263	1655	1329	6.8	5.2	822	647	876	679	6.6	5.0
934	759	1000	801	7.0	5.5	1501	1318	1607	1401	7.1	6.3
745	618	793	650	6.5	5.2	537	436	572	458	6.5	5.1
577	486	615	512	6.7	5.5	600	525	639	556	6.6	5.9
429	358	455	376	6.0	5.2	209	165	221	173	5.8	4.7
280	234	297	247	6.2	5.4	341	301	361	318	6.0	5.5

Table 4.
Comparison of results between SIMPACK® and the current method—Lines 13.

4. Conclusions

A simple truss-based finite element method was proposed to simulate the load distributions and geometric configurations of assemblies that behave in a catenary-like manner, subject to external, variable loads. The formulation was tailored to the particular problem of log booms (structures that retain logs from reaching the machinery of hydropower plants) under the influence of river streams and the logs they convey. The nonlinear formulation imposes equilibrium between internal and external forces so that an iterative scheme must be numerically solved. The method was verified by comparison against analytical results from a theoretical catenary model: the relative error and uncertainty for the maximum and minimum forces were within 0.2%, while the mesh refinement order of convergence was close to 1. The tool was later validated against experimental model-scale data from the towing tank at the Institute for Technological Research [12] and prototype-scale numerical data from commercial software SIMPACK®, and all the results agree adequately [14]: for the experimental data validation, the numerical method was capable of reproducing the observations of the experiments, and the maximum relative discrepancy observed was about 6%. The differences are invariant to the increase in the assembly length, but they seem sensible to variations of the free stream. Likewise, the prototype-scale validations all show adequate agreement, regardless of the line configurations, and a maximum relative error, considering SIMPACK® as the reference, of less than 8%. These percentages corroborate the adequacy of the method for the purpose by which it was developed: to a have a fast, yet reliable,

tool, to forecast the tension distributions throughout the lines such that it can be used as a simulator for the assessment of the structural safety of log boom assemblies.

Acknowledgements

Author details

Jose Rodolfo Chreim* and Joao Lucas Dozzi Dantas
Institute for Technological Research, Sao Paulo, Brazil

*Address all correspondence to: jrchreim@outlook.com

IntechOpen

References

[1] The Ocean Cleanup. The Ocean Cleanup Technology; 2019. Accessed date: 12/Apr/2018. Available from: https://theoceancleanup.com/technology/

[2] Felippa CA. Introduction to Finite Element Methods. Boulder: Department of Aerospace Engineering Sciences, University of Colorado; 2004

[3] Gavin H. Geometric Stiffness Effects in 2D and 3D Frames. Department of Civil and Environment Engineering, Edmund T. Pratt School of Engineering, Duke University; 2012. Accessed date: 12/Apr/2018. Available from: http://people.duke.edu/~hpgavin/cee421/frame-finite-def.pdf

[4] Neto AG, Correia RP. Ambiente de análise de risers em águas ultraprofundas: Análise estática, pré e pós-processador [Undegratuate degree thesis]. São Paulo, Brazil: Universidade de São Paulo; 2006

[5] Castro F, Katsuno E, Dantas J. Instrumentation methodology for a log containment grid model in towing tank tests. In: The 30th American Towing Tank Conference; The Society of Naval Architects and Marine Engineers; 2017

[6] Ferreira AJ. MATLAB Codes for Finite Element Analysis: Solids and Structures. Vol. 157. Netherlands: Springer Science & Business Media; 2008

[7] Katsuno ET, de Castro FS, Dantas JLD. Hydrodynamic analysis of debris containment grids in hydropower plant using porous media. In: 24th ABCM International Congress of Mechanical Engineering (COBEM 2017); ABCM - Associacao Brasileira de Engenharia e Ciencias Mecanicas; 2017

[8] Katsuno ET, de Castro FS, Dantas JLD. Debris containment grid CFD validation with towing tank tests. In: The 30th American Towing Tank Conference; The Society of Naval Architects and Marine Engineers; 2017

[9] Katsuno ET, de Castro FS, Assi GRS, Dantas JLD. Numerical analysis of debris containment grid fluid-body interaction. In: ASME 2018 37th International Conference on Ocean, Offshore and Arctic Engineering; American Society of Mechanical Engineers; 2018

[10] de Castro FS, Katsuno ET, Assi GRS, Dantas JLD. Structural investigation of the log accumulation in a debris containment grid through towing tank experiments. In: ASME 2018 37th International Conference on Ocean, Offshore and Arctic Engineering; American Society of Mechanical Engineers; 2018

[11] V&V20 Committee et al. Standard for Verification and Validation in Computational Fluid Dynamics and Heat Transfer. New York: The American Society of Mechanical Engineers; 2009

[12] Chreim JR, Dantas JLD, Lima AA. Nonlinear truss-based quasi-static structural model for force distribution predictions on debris containment grids. In: ASME 2018 37th International Conference on Ocean, Offshore and Arctic Engineering; American Society of Mechanical Engineers; 2018

[13] de Castro FS, Katsuno ET, de Souza JMP, Kogishi AM, Dantas JLD. Structural analysis for a reduced scale model of a hydropower plant debris containment grid. In: 24th ABCM International Congress of Mechanical Engineering (COBEM 2017); ABCM – Associacao Brasileira de Engenharia e Ciencias Mecanicas; 2017

[14] Chreim JR, Lima BM, Dantas JLD. Validation of a simple dynamical structural model for hydrodynamic loads. In: 27th International Congress on Waterborne Transportation, Shipbuilding, and Offshore Constructions; 2018